Direct Dynamics Study on the Hydrogen Abstraction Reaction $CH_2O + HO_2 \rightarrow CHO + H_2O_2$

Qian Shu Li,* Xin Zhang, and Shao Wen Zhang

The Institute for Chemical Physics, Beijing Institute of Technology, Beijing 100081, People's Republic of China

Received: August 29, 2005; In Final Form: October 17, 2005

We present a direct ab initio dynamics study on the hydrogen abstraction reaction $CH_2O + HO_2 \rightarrow CHO + H_2O_2$, which is predicted to have four possible reaction channels caused by different attacking orientations of HO_2 radical to CH_2O. The structures and frequencies at the stationary points and the points along the minimum energy paths (MEPs) of the four reaction channels are calculated at the B3LYP/cc-pVTZ level of theory. Energetic information of stationary points and the points along the MEPs is further refined by means of some single-point multilevel energy calculations (HL). The rate constants of these channels are calculated using the improved canonical variational transition-state theory with the small-curvature tunneling correction (ICVT/SCT) method. The calculated results show that, in the whole temperature range, the more favorable reaction channels are Channels 1 and 3. The total ICVT/SCT rate constants of the four channels at the HL//B3LYP/cc-pVTZ level of theory are in good agreement with the available experiment data over the measured temperature ranges, and the corresponding three-parameter expression is $k^{ICVT/SCT} = 3.13 \times 10^{-20}\ T^{2.70} \exp(-11.52/RT)$ cm^3 mole^{-1} s^{-1} in the temperature range of 250−3000 K. Additionally, the flexibility of the dihedral angle of H_2O_2 is also discussed to explain the different experimental values.

Introduction

Formaldehyde (CH_2O) and hydrogen peroxide (H_2O_2) are the key secondary products formed during the oxidation of organic compounds in the atmospheric boundary layer (ABL).[1] They also influence the oxidation capacity of the troposphere because they are important precursors of radicals such as OH and HO_2.[2] To accurately model the chemical processes in the atmosphere, either the decomposition mechanisms or the kinetics of the reactions involving these compounds are necessary.[3,4] Among them, the reaction of formaldehyde with HO_2 radical is quite important because it is one of the chain propagation steps of the decomposition mechanisms in atmosphere[3−5] and can provide an uncomplicated probe of the chemical reactivity of corresponding compounds. According to the investigation of Evleth et al.,[5] the reaction of HO_2 radical with formaldehyde can proceed via an addition reaction

$$CH_2O + HO_2 \rightarrow [CH_2OHO_2]\ \text{complex} \rightarrow \text{TS} \rightarrow OOCH_2OH$$

which is a very fast photochemical reaction and has been thoroughly investigated both experimentally[3,8] and theoretically[5] for many years.

Meanwhile, the hydrogen abstraction reaction between CH_2O and HO_2

$$CH_2O + HO_2 \rightarrow CHO + H_2O_2$$

which involves the transformation between CH_2O and H_2O_2, also plays an important role in the depletion mechanism of ozone in the stratosphere and is obviously very significant for the investigation of atmospheric chemistry. Moreover, in combustion chemistry, this hydrogen abstraction reaction has been proven to be indispensable[10] in the pyrolysis and oxidation mechanisms of formaldehyde, which has long been recognized as a critical kinetic intermediate in the oxidation of hydrocarbon fuels,[6,7] especially methane and methanol.[6]

Unfortunately, despite the admitted importance of this hydrogen abstraction reaction, there is still very limited information of direct experimental studies[4] on this gas-phase reaction because of the difficulty of finding suitable HO_2 radical sources.[17] However, over the past 40 years, many investigations[7,9−19] on formaldehyde pyrolysis and oxidation have concerned the title reaction, and several rate constant expressions[7,9,13−15,18] have been estimated. In a recent work, Eiteneer et al.[9] deduced an Arrhenius expression $k = 1.05 \times 10^{-13}\ (T/298)^{2.50} \exp(-5136/T)$ cm^3 mole^{-1} s^{-1} at the temperature range of 641−1600 K. But to the best of our knowledge, little theoretical attention has been paid to this reaction.

In this study, we report a direct ab initio dynamics[28] study on the hydrogen abstraction reaction of formaldehyde with HO_2 radical. We have considered all the reaction possibilities caused by the different attacking orientations of HO_2 radical to CH_2O. Additionally, the calculated results show that there is a distinct discrepancy between our predicted dihedral angle of H_2O_2 and some experimental ones, so the flexibility of the dihedral angle of H_2O_2 is also further discussed to explain the different experimental values.[34,35]

Methodology

A. Rate Constant Calculations. The improved canonical variational transition-state theory (ICVT),[20] implemented with features from microcanonical ensemble, is a modification to the canonical variational transition-state theory (CVT)[21,22] and is more accurate than the latter for calculations of rate constants of low temperatures where the contribution from the threshold region is important. Within the framework of ICVT, the

* Corresponding author. Fax: +86-10-68912665. E-mail: qsli@bit.edu.cn.

10.1021/jp054884q CCC: $30.25
Published on Web 11/22/2005

improved generalized transition-state rate constant, $k^{IGT}(T, s)$, can be calculated at the reaction coordinate s along the minimum energy path (MEP) at a fixed temperature; then the ICVT rate constant is obtained by minimizing $k^{IGT}(T, s)$ along the MEP at the given temperature as follows:

$$k^{ICVT}(T) = \min_s k^{IGT}(T,s)$$

in which

$$k^{IGT}(T,s) = [h\phi^{R}(T)]^{-1}\int_{V_a^G}^{\infty} e^{-\beta E} N^{GT}(E,s)\mathrm{d}E$$

where h is Planck's constant, $\phi^R(T)$ is the reactant partition function per unit volume, $\beta = 1/(k_B T)$, k_B is Boltzmann's constant, V_a^G is the vibrationally adiabatic ground-state potential energy at s, and $N^{GT}(E, s)$ is the quantized cumulative reaction probability at energy E and reaction coordinate s.

Furthermore, in the present study, the ICVT rate constants are also corrected with the small-curvature tunneling (SCT) correction method proposed by Truhlar and co-workers,[22] which is based on the centrifugal dominant small-curvature semiclassical ground-state (CD-SCSAG) method and takes the quantum effects along the reaction coordinate into consideration. For the purpose of comparison, the calculations of the reaction rate constants are also carried out by using the conventional transition-state theory (TST) and the Rice−Ramsperger−Kassel−Marcus (RRKM) theory[23] coupled with the Eckart tunneling correction (RRKM/Eckart).

It should be mentioned that the normal-mode frequency analysis failed to correctly predict the frequencies along the MEPs in this study. Thus, the redundant curvilinear reaction coordinate is adopted in the calculations of rate constants to reproduce the frequencies.[25] And in this study, the evaluations of the TST, ICVT, and ICVT/SCT rate constants are performed employing the POLYRATE 8.2[25] program, while the RRKM/Eckart rate constants are calculated using the online VKLab program package.[24]

B. Electronic Structure Calculations. By means of the GAUSSIAN03 program,[26] ab initio and density functional theory (DFT) calculations are carried out for stationary points (reactants, transition states, and products) and for MEPs in an effort to obtain electronic structure information for these reaction channels. The geometries of the stationary points are fully optimized employing the hybrid functional B3LYP[27] method with Dunning's[29] correlation consistent polarized valence triple-ζ basis set, namely, the cc-pVTZ basis set. Here, B3LYP refers to the combination of the Becke's three-parameter exchange with the Lee−Yang−Parr (LYP) correlation functional. The frequencies are calculated at the same level. Meanwhile, QCISD/cc-pVTZ[30] is also used to calculate the stationary point properties of these channels for comparison. The MEPs are obtained at the B3LYP/cc-pVTZ level of theory from $s = -2.00$ to 2.00 $(amu)^{1/2}$ bohr using the intrinsic reaction coordinate (IRC) method with a step size of 0.01 $(amu)^{1/2}$ bohr in mass-weighted Cartesian coordinates. The harmonic vibrational frequencies as well as the Hessian matrixes at the selected points along the MEPs are calculated at the same level. It's well known that the energies of the MEP constructed by the DFT method are not always sufficiently accurate for rate constant calculation. To yield a more reliable energy and shape of the MEP, the single-point energies of all stationary points and the points along the MEPs are further refined by means of some single-point multilevel energy calculations (HL) based on the optimized geometries at the B3LYP/cc-pVTZ level of theory. The HL[31] method employs a combination of QCISD(T) and MP2, and the calculations can be expressed as

$$\begin{aligned} E_{HL} = {} & E[\text{QCISD(T)/cc-pVTZ}] + \{E[\text{QCISD(T)/cc-pVTZ}] - E[\text{QCISD(T)/cc-pVDZ}]\}0.46286 + E[\text{MP2/cc-pVQZ}] + \{E[\text{MP2/cc-pVQZ}] - E[\text{MP2/cc-pVTZ}]\}0.69377 - E[\text{MP2/cc-pVTZ}] - \{E[\text{MP2/cc-pVTZ}] - E[\text{MP2/cc-pVDZ}]\}0.46286 \end{aligned}$$

Here, QCISD(T) denotes the quadratic configuration interaction calculation, including single and double substitutions with a triple contribution to the energy added,[30] and MP2 stands for the second-order Møller−Plesset perturbation theory with frozen core approximation. The terms cc-pVDZ and cc-pVQZ correspond to Dunning's correlation consistent polarized valence double-ζ and quadruple-ζ basis sets,[29] respectively. In addition, the single-point energies of stationary points at the CCSD(T)/cc-pVTZ//B3LYP/cc-pVTZ and G2MP2//QCISD/cc-pVTZ levels of theory are also calculated for comparison.

C. Average Dihedral Angle Calculations. In the framework of statistical thermodynamics,[43] if the property A of a system changes as a function of variable ξ, its average value is

$$\bar{A} = \sum_i A(\xi_i) \cdot w_A(\xi_i) \qquad \text{(i)}$$

where $w_A(\xi_i)$ is the probability of the value of A at a certain ξ. According to the Boltzmann distribution law

$$w_A(\xi_i) = \frac{1}{Q} \mathrm{e}^{-\beta \cdot E(\xi_i)} \qquad \text{(ii)}$$

in which $E(\xi)$ refers to the energy of a system as a function of ξ, the constant $\beta = 1/(k_B T)$, k_B is Boltzmann's constant, and Q is the partition function of the system

$$Q = \sum_i \mathrm{e}^{-\beta \cdot E(\xi_i)} \qquad \text{(iii)}$$

In the case of hydrogen peroxide, H_2O_2, the energy of the system changes as a function of a dihedral angle Φ. According to eq ii, the probability of a dihedral angle Φ at its certain value φ can be obtained at a specific temperature T. Once the torsion potential energy curve of the dihedral angle Φ is given, the probability $w_\Phi(\varphi)$ at each φ will be known. Then employing eq i, we can acquire the average dihedral angle $\bar{\Phi}$ of H_2O_2 at the given temperature T. In the present study, the average dihedral angle is calculated at 298 K, the temperature at which the experimental data is measured.

Results and Discussion

During the calculation, four different attacking orientations of HO_2 radical to CH_2O were found; correspondingly, four different transition states (Figure 1) as well as four different possible channels for the title reaction were obtained as follows:

$$CH_2O + HO_2 \rightarrow \textit{cis}\text{-TS(a)} \rightarrow CHO + H_2O_2\text{(a)} \qquad (1)$$

$$CH_2O + HO_2 \rightarrow \textit{trans}\text{-TS(a)} \rightarrow CHO + H_2O_2\text{(a)} \qquad (2)$$

$$CH_2O + HO_2 \rightarrow \textit{cis}\text{-TS(b)} \rightarrow CHO + H_2O_2\text{(b)} \qquad (3)$$

$$CH_2O + HO_2 \rightarrow \textit{trans}\text{-TS(b)} \rightarrow CHO + H_2O_2\text{(b)} \qquad (4)$$

As shown in Figure 1, the transition states *cis*-TS(a) and *cis*-TS(b) are mirror images of each other, as are *trans*-TS(a) and

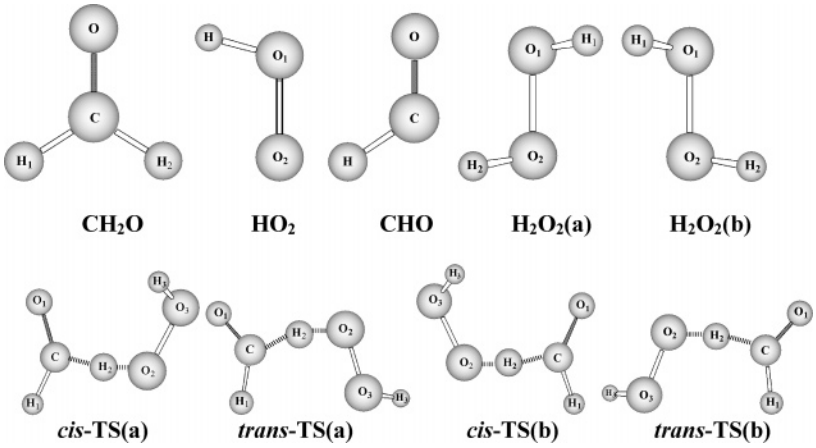

Figure 1. Conformations of reactants (CH_2O and HO_2) and products (CHO and stable stereoisomers of H_2O_2) and structures of possible transition states for the title reaction. See Tables 1 and 2 for complete list of geometrical parameters.

TABLE 1: Optimized Geometrical Parameters (Distances in Å and Angles in deg) of All the Reactants and Products at the B3LYP/cc-pVTZ and QCISD/cc-pVTZ Levels

	geometrical parameter	B3LYP/ cc-pVTZ	QCISD/ cc-pVTZ	exptl
CH_2O	$r(C-H_1)$	1.107	1.102	1.099 ± 0.009[a]
	$r(C-H_2)$	1.107	1.102	1.099 ± 0.009
	$r(C-O)$	1.199	1.205	1.203 ± 0.003
	$\theta(O-C-H_1)$	122.1	121.9	121.8
	$\theta(H_1-C-H_2)$	115.7	116.2	116.5 ± 1.2
	$\Phi(O-C-H_1-H_2)$	180.0	180.0	180.0
HO_2	$r(H-O_1)$	0.975	0.969	0.971 ± 0.002[b]
	$r(O_1-O_2)$	1.329	1.334	1.331 ± 0.001
	$\theta(H-O_1-O_2)$	105.2	104.0	104.29 ± 0.31
CHO	$r(C-O)$	1.173	1.178	1.175 ± 0.002[c]
	$r(C-H)$	1.124	1.118	1.119 ± 0.005
	$\theta(O-C-H)$	124.3	124.8	124.43 ± 0.25
H_2O_2(a)	$r(H_1-O_1)$	0.966	0.961	0.965 ± 0.005[d]
	$r(O_1-O_2)$	1.452	1.442	1.464 ± 0.003
	$r(O_2-H_2)$	0.966	0.961	0.965 ± 0.005
	$\theta(H_1-O_1-O_2)$	100.4	100.2	99.04 ± 1.20
	$\theta(O_1-O_2-H_2)$	100.4	100.2	99.04 ± 1.20
	$\Phi(H_1-O_1-O_2-H_2)$	113.9	112.9	120.3 ± 0.7 (111.9 ± 0.4)[e]
H_2O_2(b)[f]	$\Phi(H_1-O_1-O_2-H_2)$	−113.9	−112.9	-120.3 ± 0.7 (-111.9 ± 0.4)[e]

[a] Ref 32. [b] Ref 36. [c] Ref 33. [d] Ref 34. [e] Ref 35. [f] The other geometrical parameters are the same as those for H_2O_2(a).

TABLE 2: Optimized Geometrical Parameters (Distances in Å and Angles in deg) of the Transition-State Structures at the B3LYP/cc-pVTZ and QCISD/cc-pVTZ Levels

	geometrical parameter	B3LYP/ cc-pVTZ	QCISD/ cc-pVTZ
cis-TS(a)	$r(C-H_1)$	1.115	1.106
	$r(C-H_2)$	1.330	1.294
	$r(C-O_1)$	1.182	1.200
	$r(H_2-O_2)$	1.208	1.228
	$r(O_2-O_3)$	1.402	1.423
	$r(O_3-H_3)$	0.968	0.971
	$\theta(H_1-C-H_2)$	115.4	116.5
	$\theta(O_1-C-H_2)$	121.0	119.1
	$\theta(C-H_2-O_2)$	175.2	167.8
	$\theta(H_2-O_2-O_3)$	104.3	101.6
	$\theta(O_2-O_3-H_3)$	102.9	102.2
	$\Phi(H_1-H_2-C-O_1)$	−179.6	−179.4
	$\Phi(O_1-C-H_2-O_2)$	5.1	−4.3
	$\Phi(C-H_2-O_2-O_3)$	−26.3	−24.4
	$\Phi(H_2-O_2-O_3-H_3)$	95.4	95.8
trans-TS(a)	$r(C-H_1)$	1.116	1.108
	$r(C-H_2)$	1.315	1.274
	$r(C-O_1)$	1.180	1.199
	$r(H_2-O_2)$	1.225	1.254
	$r(O_2-O_3)$	1.406	1.428
	$r(O_3-H_3)$	0.968	0.970
	$\theta(H_1-C-H_2)$	110.8	110.5
	$\theta(O_1-C-H_2)$	125.2	124.4
	$\theta(C-H_2-O_2)$	170.6	165.6
	$\theta(H_2-O_2-O_3)$	104.0	101.4
	$\theta(O_2-O_3-H_3)$	102.6	101.8
	$\Phi(H_1-H_2-C-O_1)$	179.2	180.0
	$\Phi(O_1-C-H_2-O_2)$	177.9	−173.8
	$\Phi(C-H_2-O_2-O_3)$	10.0	10.8
	$\Phi(H_2-O_2-O_3-H_3)$	100.7	103.8
cis-TS(b)[a]	$\Phi(H_1-H_2-C-O_1)$	179.6	179.4
	$\Phi(O_1-C-H_2-O_2)$	−5.1	4.3
	$\Phi(C-H_2-O_2-O_3)$	26.3	24.4
	$\Phi(H_2-O_2-O_3-H_3)$	−95.4	−95.8
trans-TS(b)[b]	$\Phi(H_1-H_2-C-O_1)$	−179.2	0.0
	$\Phi(O_1-C-H_2-O_2)$	−177.9	173.8
	$\Phi(C-H_2-O_2-O_3)$	−10.0	−10.8
	$\Phi(H_2-O_2-O_3-H_3)$	−100.7	−103.8

[a] The other geometrical parameters are the same as those for *cis*-TS(a) [b] The other geometrical parameters are the same as those for *trans*-TS(a)

trans-TS(b), which leads to the equivalence between Channels 1 and 3 as well as Channels 2 and 4. Therefore, in this article, the detailed calculating information is mainly provided for Channels 1 and 2 as well as the species involved.

A. Stationary Points. The optimized geometric parameters of all the reactants, products, and transition states at the B3LYP/cc-pVTZ and QCISD/cc-pVTZ levels of theory along with the available experimental data[32−36] are given in Tables1 and 2; the corresponding conformations are shown in Figure 1. For all species listed in Table 1, the calculated structural parameters at the B3LYP/cc-pVTZ level of theory are very close to the ones at the higher level of QCISD/cc-pVTZ. Meanwhile, the results at both the levels are in good agreement with the experimental values,[32−36] indicating that these two methods are suitable to depict the structures involved in this reaction.

For the dihedral angle Φ of product H_2O_2, there is uncertainty about the comparison between our calculation and the experiment because there are two sets of different experimental values ($120.3 \pm 0.7°$ from Dorofeeva et al.[34] and $111.9 \pm 0.4°$ determined by Flaud et al.[35]) at 298 K. Our calculated results in the present article (113.9° at the B3LYP/cc-pVTZ level and 112.9° at the QCISD/cc-pVTZ level) seem more similar to the latter experimental value. To look into this puzzling problem, the profiles of the potential energy for the internal torsion of dihedral angle HOOH were calculated at the B3LYP/cc-pVTZ and QCISD/cc-pVTZ levels, respectively. (The dihedral angle is scanned at an interval of 10°, and the rest of the geometric

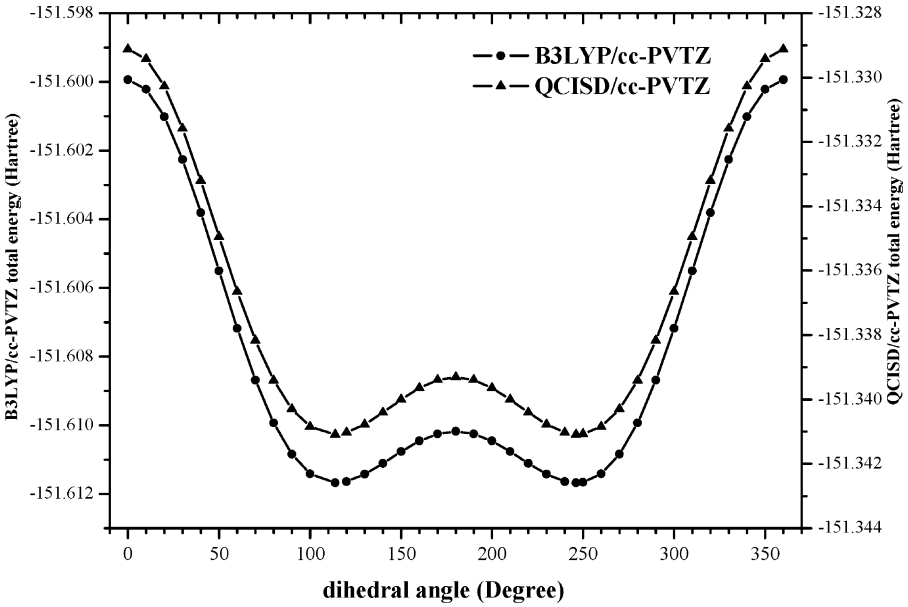

Figure 2. Calculated potential energies as functions of the dihedral angle Φ ($H_1-O_1-O_2-H_2$) of H_2O_2 at the B3LYP/cc-pVTZ and QCISD/cc-pVTZ levels of theory: (●) B3LYP/cc-pVTZ, and (▲) QCISD/cc-pVTZ.

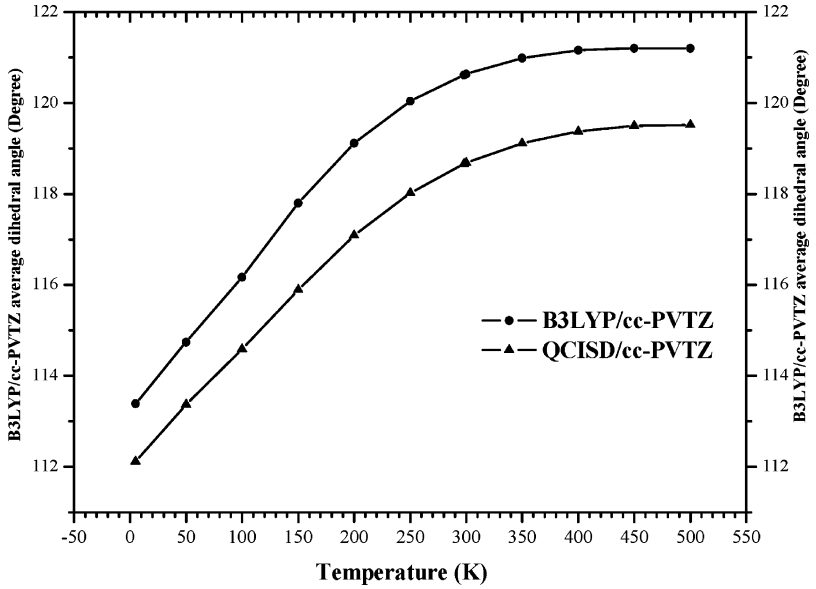

Figure 3. Calculated average dihedral angles of H_2O_2 as functions of temperature at the B3LYP/cc-pVTZ and QCISD/cc-pVTZ levels of theory: (●) B3LYP/cc-pVTZ, and (▲) QCISD/cc-pVTZ.

parameters are fully relaxed to minimize the energy of the system.) The result is shown in Figure 2. Evidently, the barriers associated with the torsion dihedral angle are very low, and both torsion potential energy curves are symmetrical with respect to the dihedral at 180°. Each side of the symmetric potential curve presents a stereoisomer of H_2O_2 as shown in Figure 1. In the range of 0−180°, The potential minimums are located at the dihedral angle of 113.9° at the B3LYP/cc-pVTZ level and 112.9° at the QCISD/cc-pVTZ level, which are just the dihedral angles of stationary point H_2O_2 at the two levels of theory, respectively. On the basis of the two torsion potential energy curves and employing the statistical thermodynamics method described in eqs i−iii, the average dihedral angle $\bar{\Phi}$ of H_2O_2 is calculated to be 120.6° at the B3LYP/cc-pVTZ level and 118.7° at the QCISD/cc-pVTZ level at 298 K, which is in good agreement with the experimental value of 120.3 ± 0.7° at the same temperature. Furthermore, we also calculated a series of average dihedral angles of H_2O_2 at different temperatures, and the results are shown in Figure 3. It can be seen that the $\bar{\Phi}$ at ∼0 K at the two levels of theory are respectively very similar to the dihedral angles corresponding to the potential minimum in Figure 2, which implies that the internal torsion of the dihedral angle nearly disappears at very low temperatures. As the temperature rises in the range of 0−500 K, the average dihedral angle almost linearly increases to the inflection (∼120.5° at the B3LYP/cc-pVTZ level and ∼118.5° at the QCISD/cc-pVTZ level) at about 300 K, then it becomes insensitive to the change of temperature. This result indicates that the rising of temperature will increase the average torsion angle at low temperatures, and, after a specific temperature, the average torsion angle reaches thermodynamic equilibrium and stays unchanged with the increase of temperature. So it can be deduced that the calculated dihedral angles of H_2O_2 at the B3LYP/cc-pVTZ and QCISD/cc-pVTZ levels of theory are actually reasonable; the experimental value of 111.9 ± 0.4° is only the dihedral angle located at the potential minimum, whereas, because of the low torsion potential barriers, the experimental value of 120.3 ± 0.7° is the average dihedral angle of H_2O_2.

TABLE 3: Harmonic Vibrational Frequencies (cm^{-1}) of the Equilibria and Transition States at the B3LYP/cc-pVTZ and QCISD/cc-pVTZ Levels, and Zero-Point Energies (kcal/mol) at the B3LYP/cc-pVTZ Level

	harmonic vibrational frequencies			
	B3LYP/cc-pVTZ	QCISD/ cc-pVTZ	exptl	ZPE
CH_2O	1203, 1268, 1536, 1824, 2878, 2932	1213, 1287, 1556, 1816, 2953, 3019	1191, 1287, 1563, 1764, 2944, 3009[a]	16.64
HO_2	1161, 1432, 3603	1130, 1452, 3718	1101, 1389, 3413[b] 8.86	
CHO	1108, 1936, 2642	1141, 1911, 2724	1126, 1920, 2790[c]	8.13
H_2O_2(a)	370, 954, 1323, 1438, 3765, 3766	381, 969, 1354, 1465, 3847, 3848	..., 875, 1266, 1388, 3599, 3611[d]	16.61
H_2O_2(b)	same as H_2O_2(a)			
cis-TS(a)	65, 78, 291, 389,465, 540, 1012, 1106, 1211, 1393, 1539, 1883, 2794, 3716, 1632i	74, 90, 271, 406, 495, 594, 974, 1140, 1250, 1397, 1576, 1853, 2973, 3789, 2527i		23.56
trans-TS(a)	56, 98, 277, 334, 464, 576, 1002, 1117, 1200, 1385, 1557, 1895, 2782, 3719, 1605i	50, 97, 269, 368, 488, 593, 962, 1146, 1241, 1386, 1601, 1863, 2960, 3793, 2430i		23.53
cis-TS(b)	same as *cis*-TS(a)			
trans-TS(b)	same as *trans*-TS(a)			

[a] ref 37. [b] ref 39. [c] ref 38. [d] ref 34.

For transition states, all the optimized geometries have C_1 symmetry. Figure 1 shows that the geometric structure $O_1-C-O_2-O_3$ is a cis structure in the transition states *cis*-TS(a) and *cis*-TS(b), whereas it is a trans structure in *trans*-TS(a) and *trans*-TS(b). As mentioned in the beginning, *cis*-TS(a) and *cis*-TS(b) are mirror images of each other, as are *trans*-TS(a) and *trans*-TS(b). In all transition-state structures, the three atoms involved in the bond-breaking-and-bond-forming process are nearly collinear. At the B3LYP/cc-pVTZ level of theory, the

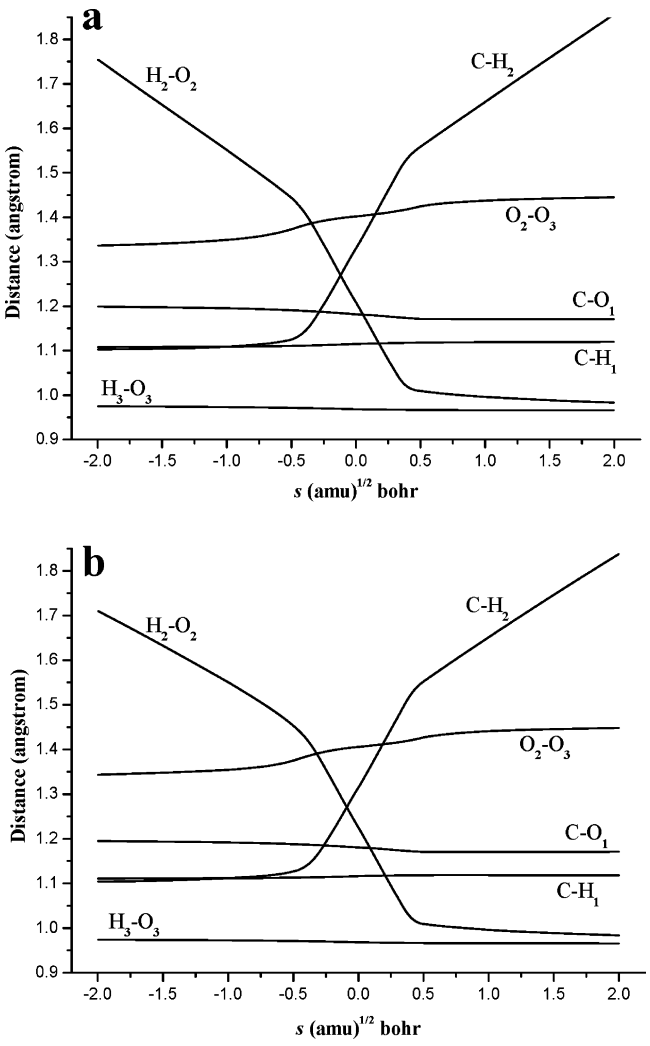

Figure 4. Changes in the bond lengths (in Å) as functions of s [$(amu)^{1/2}$ bohr] at the B3LYP/cc-pVTZ level. (a) Channel 1 (or Channel 3), (b) Channel 2 (or Channel 4)

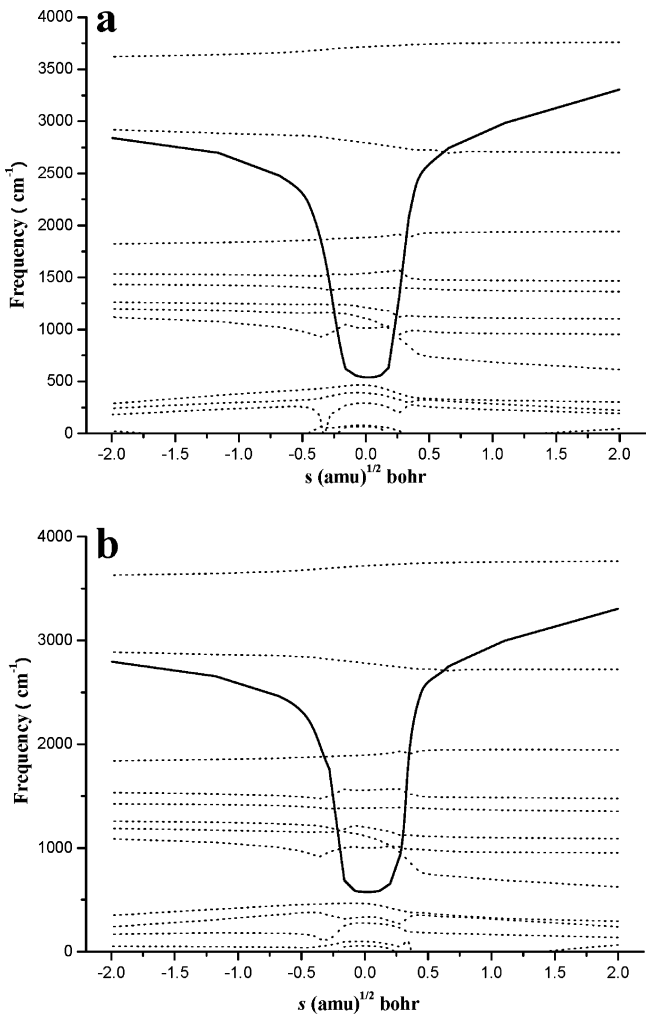

Figure 5. Changes of the generalized normal-mode vibrational frequencies as functions of s [$(amu)^{1/2}$ bohr] at the B3LYP/cc-pVTZ level. (a) Channel 1 (or Channel 3), (b) Channel 2 (or Channel 4)

TABLE 4: Reaction Enthalpies (ΔH^0_{298}) and Potential Barriers (ΔV) (kcal/mol) for the Possible Channels

	Channel 1 or 3		Channel 2 or 4	
	ΔH^0_{298}	ΔV	ΔH^0_{298}	ΔV
B3LYP/cc-pVTZ	4.06	6.87	4.06	7.06
CCSD(T)//B3LYP[a]	1.87	12.52	1.87	12.85
G2MP2//QCISD[b]	1.20	12.06	1.20	12.39
HL//B3LYP[c]	0.72	11.77	0.72	12.21
Experiment				
ΔH^0_{298}	0.53[d]			
E_a	10.21[e], 13.08[f], 11.66[g]			

[a] CCSD(T)//B3LYP denotes CCSD(T)/cc-pVTZ//B3LYP/cc-pVTZ [b] G2MP2//QCISD denotes G2MP2//QCISD/cc-pVTZ [c] HL//B3LYP denotes HL//B3LYP/cc-pVTZ [d] derived from the experimental standard formation enthalpies [e] Ref 9. [f] Ref 13. [g] Ref 15.

lengths of the breaking C−H bonds in *cis*-TS(a) and *trans*-TS(a) (which are the same as those in *cis*-TS(b) and *trans*-TS(b)) are 1.330 and 1.315 Å, respectively; whereas, the lengths of the forming H−O bonds are 1.208 Å and 1.225 Å, respectively. Compared to the corresponding equilibrium lengths, the values of these bond lengths imply that all the transition states are located in the middle of the MEPs.

The harmonic vibrational frequencies and zero-point energies (ZPE) of all the stationary points at the B3LYP/cc-pVTZ and QCISD/cc-pVTZ levels of theory along with the available experimental data[34,37−39] are listed in Table 3, which shows that the frequencies at the B3LYP/cc-pVTZ level of theory are similar to the ones calculated at the higher QCISD/cc-pVTZ level, and all of them are close to the experimental data, with the maximum relative error (about 9%) being at the frequency 954 cm^{-1} of H_2O_2 at the B3LYP/cc-pVTZ level compared with the experimental value 875 cm^{-1}. All the transition states have only one imaginary frequency, of which the absolute values at the B3LYP/cc-pVTZ level for *cis*-TS(a) and *trans*-TS(a) (which are the same as those for *cis*-TS(b) and *trans*-TS(b)) are 1632 and 1605 cm^{-1}, respectively. The large values of the imaginary frequencies imply the tunneling effect is important at low temperatures for these reaction channels.

The reaction enthalpies (ΔH^0_{298}) and potential barriers calculated at the four different levels of theory, B3LYP/cc-pVTZ, CCSD(T)/cc-pVTZ//B3LYP/cc-pVTZ, G2MP2//QCISD/cc-pVTZ, and HL//B3LYP/cc-pVTZ, are collected in Table 4, which reveal that the title reaction has very low positive reaction enthalpy and is therefore weakly endothermal. Compared to the experimental ΔH^0_{298} of 0.53 kcal/mol derived from the experimental standard formation enthalpies (H_2O_2: −32.53;[41] CHO: 10.40;[41] CH_2O: −25.96;[40] and HO_2: 3.30 kcal/mol[42]), the reaction enthalpies of all the reaction channels calculated at the B3LYP/cc-pVTZ level are obviously overestimated, while the latter three levels provide reasonable values. The calculated result at the HL//B3LYP/cc-pVTZ level of theory is especially in good agreement with the experimental reaction enthalpy. Therefore, the HL//B3LYP/cc-pVTZ method is adopted for the following calculations.

B. Reaction Path Properties. Figure 4 shows the changes of the bond lengths for all reaction channels along the MEPs as functions of the reaction coordinate *s* at the B3LYP/cc-pVTZ level. In the course of reaction, the lengths of the breaking bond $C-H_2$ and the forming bond H_2-O_2 change significantly, while the change in the other bond lengths is small, which is very similar for all the four channels. As the reaction proceeds to products, the length of the breaking bond $C-H_2$ remains insensitive up to $s = -0.5$ and then increases quickly. Meanwhile, the forming bond H_2-O_2 rapidly shortens from the reactants and arrives at the corresponding equilibrium H−O bond length of the H_2O_2 at about $s = 0.5$.

The changes of the generalized normal-mode vibrational frequencies of the four channels along the MEPs as functions of *s* at the B3LYP/cc-pVTZ level are presented in Figure 5. The frequencies are associated with the reactants $CH_2O + HO_2$ in the limit of negative *s* and with the products $CHO + H_2O_2$

TABLE 5: Rate Constants (cm^3 $molecule^{-1}$ s^{-1}) of Channels 1−4 in the Temperature Range of 250−3000 K at the HL//B3LYP/cc-pVTZ Level

	Channel 1 or Channel 3				Channel 2 or Channel 4					
T(K)	TST	RRKM/E[a]	ICVT	ICVT/SCT	TST	RRKM/E	ICVT	ICVT/SCT	sum of ICVT/SCT rate constant	exptl[b]
250	2.55×10^{-24}	6.82×10^{-22}	3.70×10^{-24}	1.22×10^{-22}	1.06×10^{-24}	2.43×10^{-22}	5.29×10^{-25}	1.75×10^{-23}	2.79×10^{-22}	
350	4.35×10^{-21}	4.52×10^{-20}	5.82×10^{-21}	3.30×10^{-20}	2.33×10^{-21}	2.16×10^{-20}	1.31×10^{-21}	7.43×10^{-21}	8.09×10^{-20}	
450	3.34×10^{-19}	1.27×10^{-18}	3.87×10^{-19}	1.10×10^{-18}	2.06×10^{-19}	7.14×10^{-19}	1.17×10^{-19}	3.32×10^{-19}	2.86×10^{-18}	
500	1.63×10^{-18}	4.78×10^{-18}	1.76×10^{-18}	4.09×10^{-18}	1.05×10^{-18}	2.84×10^{-18}	5.92×10^{-19}	1.38×10^{-18}	1.09×10^{-17}	
600	1.91×10^{-17}	4.10×10^{-17}	1.82×10^{-17}	3.26×10^{-17}	1.33×10^{-17}	2.62×10^{-17}	7.19×10^{-18}	1.29×10^{-17}	9.11×10^{-17}	8.64×10^{-17} [c]
650	5.10×10^{-17}	9.91×10^{-17}	4.59×10^{-17}	7.56×10^{-17}	3.65×10^{-17}	6.51×10^{-17}	1.93×10^{-17}	3.18×10^{-17}	2.15×10^{-16}	2.01×10^{-16} [c]
700	1.21×10^{-16}	2.17×10^{-16}	1.03×10^{-16}	1.59×10^{-16}	8.89×10^{-17}	1.46×10^{-16}	4.59×10^{-17}	7.05×10^{-17}	4.59×10^{-16}	4.41×10^{-16} [d]
773	3.61×10^{-16}	5.91×10^{-16}	2.87×10^{-16}	4.04×10^{-16}	2.73×10^{-16}	4.09×10^{-16}	1.36×10^{-16}	1.92×10^{-16}	1.19×10^{-15}	1.71×10^{-15} [e]
800	5.19×10^{-16}	8.26×10^{-16}	4.01×10^{-16}	5.58×10^{-16}	3.96×10^{-16}	5.76×10^{-16}	1.94×10^{-16}	2.70×10^{-16}	1.66×10^{-15}	1.73×10^{-15} [d]
850	9.64×10^{-16}	1.47×10^{-16}	7.14×10^{-16}	9.56×10^{-16}	7.49×10^{-16}	1.04×10^{-15}	3.59×10^{-16}	4.80×10^{-16}	2.87×10^{-15}	3.31×10^{-15} [f]
900	1.69×10^{-15}	2.48×10^{-15}	1.20×10^{-15}	1.56×10^{-15}	1.34×10^{-15}	1.78×10^{-15}	6.24×10^{-16}	8.09×10^{-16}	4.75×10^{-15}	4.86×10^{-15} [f]
950	2.84×10^{-15}	4.02×10^{-15}	1.94×10^{-15}	2.45×10^{-15}	2.26×10^{-15}	2.92×10^{-15}	1.03×10^{-15}	1.31×10^{-15}	7.51×10^{-15}	8.48×10^{-15}
1000	4.55×10^{-15}	6.28×10^{-15}	3.00×10^{-15}	3.70×10^{-15}	3.68×10^{-15}	4.60×10^{-15}	1.64×10^{-15}	2.03×10^{-15}	1.15×10^{-14}	1.26×10^{-14}
1100	1.06×10^{-14}	1.39×10^{-14}	6.52×10^{-15}	7.76×10^{-15}	8.72×10^{-15}	1.04×10^{-14}	3.73×10^{-15}	4.44×10^{-15}	2.44×10^{-14}	2.56×10^{-14}
1200	2.19×10^{-14}	2.78×10^{-14}	1.28×10^{-14}	1.48×10^{-14}	1.84×10^{-14}	2.11×10^{-14}	7.58×10^{-15}	8.77×10^{-15}	4.71×10^{-14}	4.70×10^{-14}
1400	7.35×10^{-14}	8.83×10^{-14}	4.09×10^{-14}	4.55×10^{-14}	6.33×10^{-14}	6.85×10^{-14}	2.43×10^{-14}	2.71×10^{-14}	1.45×10^{-13}	1.27×10^{-13}
1500	1.22×10^{-13}	1.44×10^{-13}	6.51×10^{-14}	7.15×10^{-14}	1.07×10^{-13}	1.13×10^{-13}	3.98×10^{-14}	4.37×10^{-14}	2.30×10^{-13}	2.94×10^{-13} [g]
1600	1.94×10^{-13}	2.24×10^{-13}	9.92×10^{-14}	1.08×10^{-13}	1.70×10^{-13}	1.77×10^{-13}	6.18×10^{-14}	6.71×10^{-14}	3.50×10^{-13}	4.30×10^{-13} [g]
1800	4.32×10^{-13}	4.85×10^{-13}	2.07×10^{-13}	2.20×10^{-13}	3.85×10^{-13}	3.90×10^{-13}	1.33×10^{-13}	1.42×10^{-13}	7.26×10^{-13}	
2000	8.51×10^{-13}	9.35×10^{-13}	3.84×10^{-13}	4.05×10^{-13}	7.69×10^{-13}	7.60×10^{-13}	2.56×10^{-13}	2.69×10^{-13}	1.35×10^{-12}	
2400	2.55×10^{-12}	2.72×10^{-12}	1.05×10^{-12}	1.08×10^{-12}	2.35×10^{-12}	2.25×10^{-12}	7.30×10^{-13}	7.52×10^{-13}	3.67×10^{-12}	
2800	6.03×10^{-12}	6.29×10^{-12}	2.32×10^{-12}	2.36×10^{-12}	5.62×10^{-12}	5.29×10^{-12}	1.66×10^{-12}	1.69×10^{-12}	8.10×10^{-12}	
3000	8.70×10^{-12}	9.00×10^{-12}	3.25×10^{-12}	3.29×10^{-12}	8.16×10^{-12}	7.61×10^{-12}	2.37×10^{-12}	2.40×10^{-12}	1.14×10^{-11}	

[a] RRKM/E denotes RRKM rate constants with the Eckart tunneling correction (RRKM/Eckart) [b] Ref 9. [c] Ref 13. [d] Ref 12. [e] Ref 16. [f] Ref 15. [g] Ref 10.

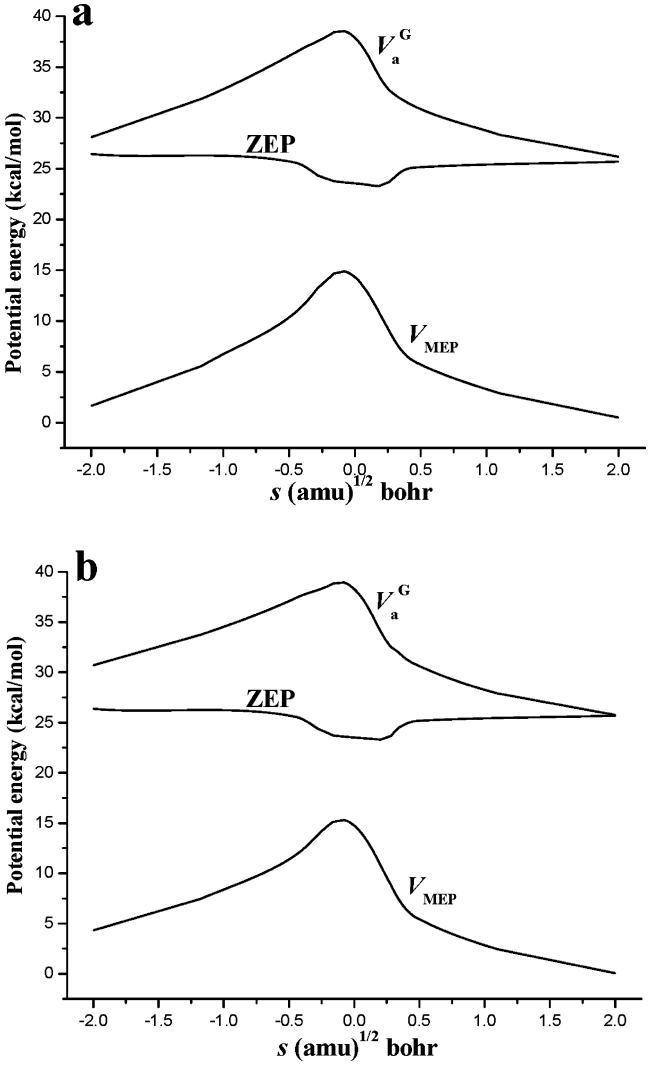

Figure 6. Classical potential energy (V_{MEP}), ZPE, and ground-state vibrationally adiabatic potential energy (V_a^G) as functions of s [(amu)$^{1/2}$ bohr] at the HL//B3LYP/cc-pVTZ level. (a) Channel 1 (or Channel 3), (b) Channel 2 (or Channel 4).

in the reverse limit. In the vicinity of the transition state (s = 0), there are fifteen vibrational frequencies, of which the frequency represented by the solid line changes strongly in the range of s from −0.5 to 0.5. When $s < 0$, this vibrational mode represents the stretching vibration of the breaking bond C−H of the molecule CH_2O; however, when $s > 0$, the stretching vibration of the forming bond H−O of the molecule H_2O_2 is related to the vibrational mode. This kind of behavior is known to be a typical feature of hydrogen abstraction reactions, and this vibrational mode can be referred to as the "reaction mode". Therefore, from the changes of bond lengths and frequencies, the "reaction region" is in the range of $s = -0.5$ to 0.5.

The classical potential energy (V_{MEP}), the ZPE, and the ground-state vibrationally adiabatic potential energy (V_a^G) as functions of s are plotted in Figure 6. For the four reaction channels, the position of the maximum value of the classical potential energy curve (V_{MEP}(s)) at the HL level of theory just corresponds to the saddle-point position (s = 0) at the B3LYP/cc-pVTZ level. Meanwhile, the maximum position of V_a^G is very close to the maximum position of V_{MEP}, and the two curves are similar in shape because the ZPE curve is practically constant as s varies only with a gentle fall near the saddle point (s = 0). This implies that the variational effect for the title reaction may not be significant to the calculations of the rate constants. In addition, according to the potential-barrier heights obtained from Figure 6 and Table 4, it is obvious that Channels 1 and 3 are favorable reaction channels compared with Channels 2 and 4.

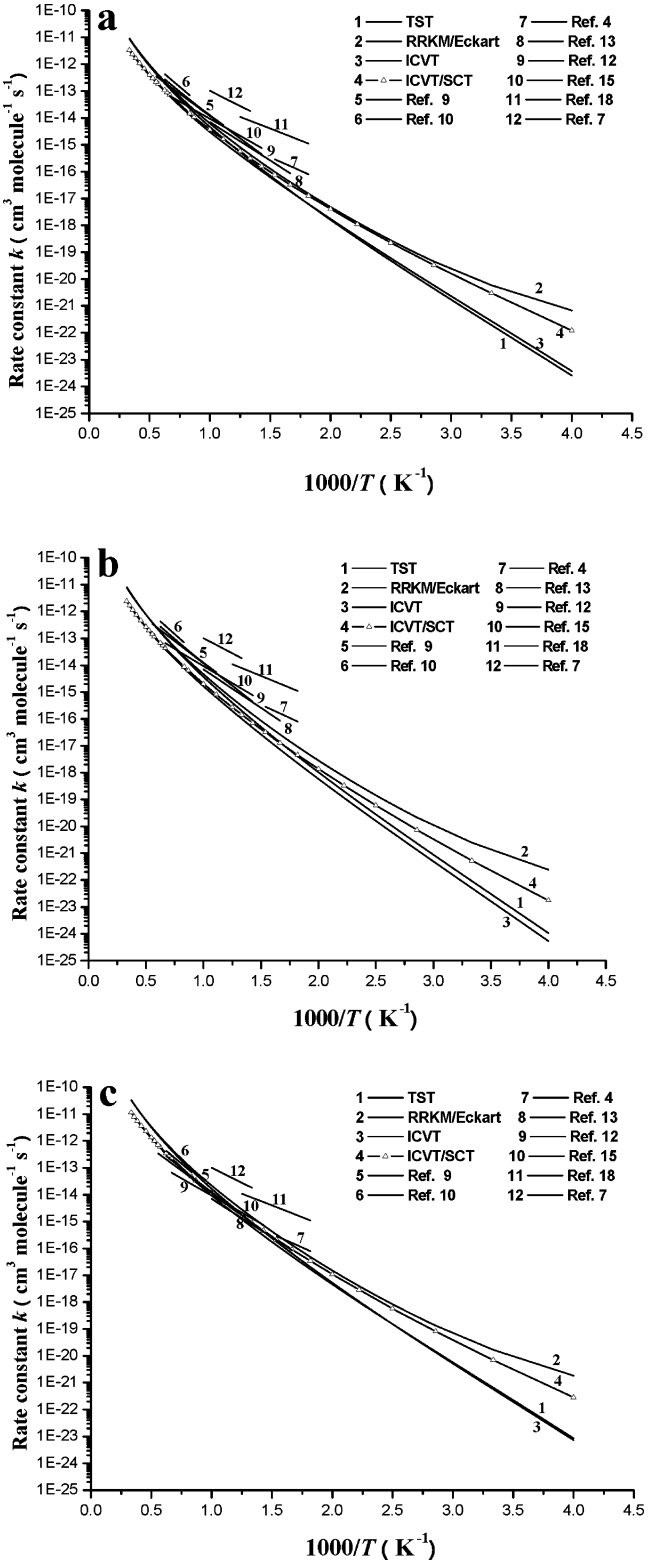

Figure 7. Plot of the IVCT/SCT, RRKM/Eckart, TST, and IVCT rate constants at the HL//B3LYP/cc-pVTZ level, and the available experimental data k (cm^3 mole^{-1} s^{-1}) vs 1000/T (K^{-1}) in the temperature range of 250−3000 K. (a) Channel 1 (or Channel 3), (b) Channel 2 (or Channel 4), (c) sum of the four reaction channels.

C. Rate Constant Calculation. The ICVT/SCT method is employed to calculate the rate constants of all the channels at the HL//B3LYP/cc-pVTZ level of theory within a wide tem-

perature range of 250−3000 K, which are listed in Table 5 along with the rate constants of the conventional TST, ICVT, and RRKM/Eckart theories for comparison. Meanwhile, to clarify the main results, both the theoretical and experimental rate constants are plotted against 1000/T (K) in Figure 7a,b, which clearly show that the rate constants of Channel 1 (or Channel 3) are larger than those of Channel 2 (or Channel 4) at the whole temperature range of 250−3000 K. Figure 7c presents the total rate constants of Channels 1−4, of which the total ICVT/SCT rate constants are well located among the experimental measurements within the temperature range in which experimental data are available. It is not difficult to find that there are only slight discrepancies between the TST and ICVT rate constants, indicating that the variational effect is very small. In addition, even though the total ICVT and total ICVT/SCT rate constants are quite similar at $T \geq 400$ K, there is still a very obvious difference between them when $T < 400$ K, which implies that the tunneling effect on the calculated reaction rate constants is very important at low temperatures. Finally, on the basis of the calculated total ICVT/SCT rate constants within 250−3000 K at the HL//B3LYP/cc-pVTZ level, a three-parameter expression $k^{\mathrm{ICVT/SCT}} = 3.13 \times 10^{-20}\, T^{2.70} \exp(-11.52/RT)$ cm^3 mole^{-1} s^{-1} is fit to describe the non-Arrhenius behavior of the rate constants within the broader temperature range.

Summary

In this paper, the hydrogen abstraction reaction $CH_2O + HO_2 \rightarrow CHO + H_2O_2$ has been investigated by a direct ab initio dynamics method. The results show that accurate geometry and frequency information can be provided at the B3LYP/cc-pVTZ level of theory, and the HL//B3LYP/cc-pVTZ method is necessary to improve the potential energy curve. The changes of the bond lengths, generalized normal-mode vibrational frequencies, and potential energies along the MEPs of all four of the possible reaction channels caused by different attacking orientations of HO_2 radical to CH_2O are very similar. The rate constants of the title reaction in the temperature range of 250−3000 K are calculated by using the ICVT/SCT method. The calculated results show that the variational effect is small, and the small-curvature tunneling effect is important within the lower temperature range. A comparison of the ICVT/SCT rate constants of each channel shows that the more favorable reaction channels are Channels 1 and 3 in the whole temperature range. And the total ICVT/SCT rate constants of all four channels at the HL//B3LYP/cc-pVTZ level of theory are in excellent agreement with the experiment data. The corresponding three-parameter expression within 250−3000 K is fit as $k^{\mathrm{ICVT/SCT}} = 3.13 \times 10^{-20}\, T^{2.70} \exp(-11.52/RT)$ cm^3 mole^{-1} s^{-1}. In addition, during the geometry optimizing of stationary point H_2O_2, our calculated dihedral angles have been proven to be reasonable, and, because of the low barriers associated with the torsion of the dihedral angle of H_2O_2, the experimental value of 111.9 ± 0.4° determined by Flaud et al. is only the dihedral angle located at the potential minimum, and the other experimental value of 120.3 ± 0.7° obtained by Dorofeeva et al. is the average dihedral angle of H_2O_2.

Acknowledgment. This work is supported by the National Science Foundation of China. Thanks are due to Professor D. G. Truhlar for providing the POLYRATE 8.2 program. We are also grateful to our reviewers for their valuable comments on the manuscript.

References and Notes

(1) Jenkin, M. E.; Clemitshaw, K. C. *Atmos. Environ.* **2000**, *34*, 2499.
(2) Crawford, J.; Davis, D.; Olson, J.; Chen, G.; Liu, S.; Gregory, G.; Barrick, J.; Sachse, G.; Sandholm, S.; Heikes, B.; Singh, H.; Blake, D. *J. Geophys. Res.* **1999**, *104*, 16255.
(3) (a) Veyret, B.; Rayez, J. C.; Lesclaux, R. *J. Phys. Chem.* **1982**, *86*, 3424. (b) Barnes, I.; Becker, K. H.; Fink, E. H.; Reiner, A.; Zabel, F.; Niki, H. *Chem. Phys. Lett.* **1985**, *115*, 1. (c) Burrows, J. P.; Moortgat, G. K.; Tyndall, G. S.; Cox, R. A.; Jenkin, M. E.; Hayman, G. D.; Veyret, B. *J. Phys. Chem.* **1989**, *93*, 2375.
(4) Jemi-Alade, A. A.; Lightfoot, P. D.; Lesclaux, R. *Chem. Phys. Lett.* **1992**, *195*, 25.
(5) Evleth, E. M.; Melius, C. F.; Rayez, M. T.; Rayez, J. C.; Forst, W. *J. Phys. Chem.* **1993**, *97*, 5040.
(6) Westbrook, C. K.; Dryer, F. L. *Prog. Energy Combust. Sci.* **1984**, *10*, 1.
(7) Vardanyan, I. A.; Sachyan, G. A.; Nalbandyan, A. B. *Combust. Flame* **1971**, *17*, 315.
(8) Veyret, B.; Lesclaux, R.; Rayez, M.-T.; Rayez, J.-C.; Cox, R. A.; Moortgat, G. K. *J. Phys. Chem.* **1989**, *93*, 2368.
(9) Eiteneer, B.; Yu, C.-L.; Goldenberg, M.; Frenklach, M. *J. Phys. Chem. A* **1998**, *102*, 5196.
(10) Hidaka, Y.; Taniguchi, T.; Tanaka, H.; Kamesawa, T.; Inami, K.; Kawano, H. *Combust. Flame* **1993**, *92*, 365.
(11) Carriere, T.; Westmoreland, P. R.; Kazakov, A.; Stein, Y. S.; Dryer, F. L. *Proc. Combust. Inst.* **2002**, *29*, 1257.
(12) Hochgreb, S.; Dryer, F. L. *Combust. Flame* **1992**, *91*, 257.
(13) Baulch, D. L.; Cobos, C. J.; Cox, R. A.; Esser, C.; Frank, P.; Just, T.; Kerr, J. A.; Pilling, M. J.; Troe, J.; Walker, R. W.; Warnatz, J. *J. Phys. Chem. Ref. Data* **1992**, *21*, 411.
(14) Hochgreb, S.; Yetter, R. A.; Dryer, F. L. *Symp. (Int.) Combust., [Proc.]* **1991**, *23*, 171.
(15) Tsang, W.; Hampson, R. F. *J. Phys. Chem. Ref. Data* **1986**, *15*, 1087.
(16) Baldwin, R. R.; Walker, R. W. *Symp. (Int.) Combust., [Proc.]* **1979**, *17*, 525.
(17) Walker, R. W. *Reaction Kinetics*; Ashmore, P. G., Ed.; The Chemical Society: London, 1975; Vol. 1, p 161.
(18) Lloyd, A. C. *Int. J. Chem. Kinet.* **1974**, *6*, 169.
(19) Hoare, D. E.; Milne, G. S. *Trans. Faraday Soc.* **1967**, *63*, 101.
(20) Garrett, B. C.; Truhlar, D. G.; Grev, R. S.; Magnuson, A. W. *J. Phys. Chem.* **1980**, *84*, 1730.
(21) Truhlar, D. G.; Garrett, B. C. *Annu. Rev. Phys. Chem.* **1984**, *35*, 159.
(22) Truhlar, D. G.; Isaacson, A. D.; Garret, B. C. *Theory of Chemical Reaction Dynamics*; Baer, M., Ed.; CRC Press: Boca Raton, FL, 1985; Vol. 4, p 65.
(23) (a) Wardlaw, D. M.; Marcus, R. A. *Chem. Phys. Lett.* **1984**, *110*, 230; *J. Chem. Phys.* **1985**, *83*, 3462. (b) Klippenstein, S. J. *J. Chem. Phys.* **1992**, *96*, 367. (c) Klippenstein, S. J.; Marcus, R. A. *J. Chem. Phys.* **1987**, *87*, 3410.
(24) Zhang, S.; Truong, T. N. *VKLab*, version 1.0; University of Utah: Salt Lake City, UT, 2001.
(25) Chuang, Y.-Y.; Corchado, J. C.; Fast, P. L.; Villa, J.; Hu, W.-P.; Liu, Y.-P.; Lynch, G. C.; Jackels, C. F.; Nguyen, K.; Gu, M. Z.; Rossi, I.; Coitino, E.; Clayton, S.; Melissas, V. S.; Lynch, B. J.; Steckler, R.; Garret, B. C.; Isaacson, A. D.; Truhlar, D. G. *POLYRATE*, version 8.2; University of Minnesota: Minneapolis, MN, 1999.
(26) Frisch, M. J.; Trucks, G. W.; Schlegel, H. B.; Scuseria, G. E.; Robb, M. A.; Cheeseman, J. R.; Montgomery, J. A., Jr.; Vreven, T.; Kudin, K. N.; Burant, J. C.; Millam, J. M.; Iyengar, S. S.; Tomasi, J.; Barone, V.; Mennucci, B.; Cossi, M.; Scalmani, G.; Rega, N.; Petersson, G. A.; Nakatsuji, H.; Hada, M.; Ehara, M.; Toyota, K.; Fukuda, R.; Hasegawa, J.; Ishida, M.; Nakajima, T.; Honda, Y.; Kitao, O.; Nakai, H.; Klene, M.; Li, X.; Knox, J. E.; Hratchian, H. P.; Cross, J. B.; Adamo, C.; Jaramillo, J.; Gomperts, R.; Stratmann, R. E.; Yazyev, O.; Austin, A. J.; Cammi, R.; Pomelli, C.; Ochterski, J. W.; Ayala, P. Y.; Morokuma, K.; Voth, G. A.; Salvador, P.; Dannenberg, J. J.; Zakrzewski, V. G.; Dapprich, S.; Daniels, A. D.; Strain, M. C.; Farkas, O.; Malick, D. K.; Rabuck, A. D.; Raghavachari, K.; Foresman, J. B.; Ortiz, J. V.; Cui, Q.; Baboul, A. G.; Clifford, S.; Cioslowski, J.; Stefanov, B. B.; Liu, G.; Liashenko, A.; Piskorz, P.; Komaromi, I.; Martin, R. L.; Fox, D. J.; Keith, T.; Al-Laham, M. A.; Peng, C. Y.; Nanayakkara, A.; Challacombe, M.; Gill, P. M. W.; Johnson, B.; Chen, W.; Wong, M. W.; Gonzalez, C.; Pople, J. A. *Gaussian03*; Gaussian, Inc.: Pittsburgh, PA, 2003.
(27) Becke, A. D. *J. Chem. Phys.* **1993**, *98*, 5648.
(28) Truhlar, D. G.; Gordon, M. S. *Science* **1990**, *249*, 491.
(29) Peterson, K. A.; Woon, D. E.; Dunning, T. H. *J. Chem. Phys.* **1994**, *100*, 7410.
(30) Pople, J. A.; Head-Gordon, M.; Raghavachari, K. *J. Chem. Phys.* **1987**, *87*, 5968.
(31) Miller, J. A.; Klippenstein, S. J. *J. Phys. Chem. A* **2003**, *107*, 2680.
(32) Yamada, K.; Nakagawa, T.; Kuchitsu, K.; Morino, Y. *J. Mol. Spectrosc.* **1971**, *38*, 70.
(33) Hirota, E. *J. Mol. Struct.* **1986**, *146*, 237.

(34) Dorofeeva, O. V.; Iorish, V. S.; Novikov, V. P.; Neumann, D. B. *J. Phys. Chem. Ref. Data* **2003**, *32*, 879.

(35) Flaud, J.-M.; Camy-Peyret, C.; Johns, J. W. C.; Carli, B. *J. Chem. Phys.* **1989**, *91*, 1504.

(36) Lubic, K. G., Amano, T.; Uehara, H.; Kawaguchi, K.; Hirota, E. *J. Chem. Phys.* **1984**, *81*, 4826.

(37) Duncan, J. L.; Mallinson, P. D. *Chem. Phys. Lett.* **1973**, *23*, 597.

(38) Murray, K. K.; Miller, T. M.; Leopold, D. G.; Lineberger, W. C. *J. Chem. Phys.* **1986**, *84*, 2520.

(39) Engdahl, A.; Nelander, B. *Phys. Chem. Chem. Phys.* **2004**, *6*, 730.

(40) Lide, D. R., Ed. *CRC Handbook of Chemistry and Physics*, 84th ed.; CRC Press: NewYork, 2003.

(41) Chase, M. W., Jr. NIST-JANAF Thermochemical Tables, 4th ed. *J. Phys. Chem. Ref. Data* **1998**, Monograph No. 9.

(42) Litorja, M.; Ruscic, B. *J. Electron Spectrosc.* **1998**, *97*, 131.

(43) Nash, L. K. *Elements of Statistical Thermodynamics*, 2nd ed.; Addison-Wesley: Reading, MA, 1974.